

## High Spatiotemporal Resolution of Magnetic Dynamics in Mn-Ni-Ga via Four-Dimensional Lorentz Microscopy

Ming Zhang,<sup>1,2</sup> Zi-An Li,<sup>1</sup> Shuaishuai Sun,<sup>1</sup> Peng Xu,<sup>1</sup> Chunhui Zhu,<sup>1</sup> Huanfang Tian,<sup>1</sup> Zhongwen Li,<sup>1</sup> Ying Zhang,<sup>1</sup> Huixin Yang,<sup>1</sup> and Jianqi Li<sup>1,2,3,\*</sup>

<sup>1</sup>*Beijing National Laboratory for Condensed Matter Physics, Institute of Physics, Chinese Academy of Sciences, Beijing 100190, China*

<sup>2</sup>*Department of Electrical and electronic Engineering, Southern University of Science and Technology, Shenzhen, Guangdong 518055, China*

<sup>3</sup>*Songshan Lake Materials Laboratory, Dongguan, Guangdong 523808, China*



(Received 5 March 2019; revised manuscript received 4 July 2019; published 18 September 2019)

High spatiotemporal resolution study of magnetic dynamic transitions in  $(\text{Mn}_{0.5}\text{Ni}_{0.5})_{65}\text{Ga}_{35}$  (hereafter referred to as Mn-Ni-Ga) is carried out using Lorentz ultrafast transmission electron microscopy (UTEM). The Lorentz UTEM images with a subpicosecond temporal and sub-50-nm spatial resolution reveal remarkable features of magnetic transient states after a femtosecond pulsed laser excitation and three successive dynamic processes involving four distinct magnetic states are evidently observed in Mn-Ni-Ga crystals. Moreover, a full reversible dynamic cycle for the photoinduced ferroparamagnetic transition in a time span of up to tens of microseconds is also examined by using nanosecond-laser-generated photoelectrons. The temporal changes of electron, spin, and lattice in the present system are qualitatively analyzed based on a three-temperature approximation. Our Lorentz UTEM observations highlight the feasibility of direct imaging ultrafast demagnetization and relevant dynamic natures in complex spin textures with a nanometer-picosecond spatiotemporal resolution.

DOI: 10.1103/PhysRevApplied.12.034037

### I. INTRODUCTION

Since the seminal work of femtosecond laser pulses induced ultrafast demagnetization in nickel film by Beau-repaire and coworkers in 1996 [1], study of the interactions between laser pulses and magnetic materials has become a significant topic in modern magnetism, resulting in many alternative concepts and phenomena [2–8]. Some prominent examples are ultrafast demagnetization [9–11], optically driven magnetization precession [3,12] and ultrafast magnetization switching [13,14]. Experimentally, ultra-short laser pulses provide unique temporal windows for exploring the rich interactions among the electrons, the spins, and the lattices of materials subjected to photoexcitation [15]. Several ultrafast magnetic spectroscopy and microscopy methods, including ultrafast optics [9,16], infrared [17], terahertz spectroscopy [18], synchrotron x-ray-based spectroscopy [10,19], or more recent x-ray free-electron lasers [20–22], have been successfully applied to probe ultrafast magnetization dynamics in femtosecond time scales.

However, not only high temporal resolution but also high spatial resolution is required in order to study the ultrafast dynamics of charges and spins in magnetic

structures that have reduced dimensions or host non-collinear complex spin textures (e.g., nanoscale magnetic skyrmions). Alternative experimental methods are emerging that combine ultrashort laser pulses with the imaging techniques in high-order harmonic radiation [23], scanning optical microscopy [24], near-field scanning imaging [25], and soft x-ray microscopy [26]. Recently, Vodungbo and coworkers [27] have achieved a 100-nm spatial resolution with femtosecond soft x-ray pulses to study the laser-induced demagnetization at the individual domain level. Schmising and coworkers [21] have observed demagnetization in a magnetic domain network via time-resolved Fourier transform holography with 100-fs temporal and sub-100-nm spatial resolution. However, due to the broad beam nature of lights or x-rays, it is still a challenge for these ultrafast magnetic microscopies to further extend their spatial resolution, thus preventing a nanometer-femtosecond view of the spin dynamics in magnetic nanostructures and noncollinear complex spin textures.

On the other hand, Lorentz transmission electron microscope (TEM) has been routinely used for imaging static and *in situ* dynamic magnetic structures on nanometer length scales [28–30]. By combining laser pulses [31,32] and Lorentz TEM imaging [33–35], early attempts to develop Lorentz ultrafast TEM (UTEM) have achieved some limited success, as demonstrated by Zewail with

\*ljq@iphy.ac.cn

a nanosecond temporal resolution [33]. However, further improving the temporal resolution of Lorentz UTEM has met with many technical challenges, particularly the difficulties in obtaining sufficient pulsed electrons for direct imaging [35]. Recently, Flannigan's group [34] has been able to demonstrate a picosecond view of magnetization dynamics in FePt thin films by optimizing the collection efficiency of photoelectrons for Lorentz imaging; Ropers's group has mapped the light-induced demagnetization of a single magnetic vortex structure with improved spatiotemporal resolution [36,37].

In the present work, we explore the high spatiotemporal capability of Lorentz UTEM for direct imaging photoinduced ultrafast magnetization dynamics. By maximizing the collection efficiency of photoelectrons for ultrafast magnetic imaging, we obtain decent Lorentz images with a nanometer-picosecond spatiotemporal resolution. By interfacing a femtosecond-nanosecond (fs-ns) laser system with Lorentz TEM, we study not only the ultrafast magnetization dynamics with a picosecond temporal resolution, but also a full cycle of magnetization dynamics with a time span of microseconds. Using the fs-stroboscopic Lorentz UTEM, we experimentally demonstrate a subpicosecond view of ultrafast demagnetization and directly image the rapid alterations of domain walls in a Mn-Ni-Ga [38] specimen with a sub-50-nm spatial resolution. Three successive dynamical processes of magnetization transitions and four distinct magnetic states are evidently observed. Moreover, we use the ns-stroboscopic Lorentz UTEM to obtain a full cycle of magnetization dynamics in Mn-Ni-Ga within a time span of tens of microseconds. The reversible thermally driven ferro-to-paramagnetic transition and alterations microstructure following the thermal diffusion are also discussed.

## II. RESULTS AND DISCUSSION

We first describe our home-built UTEM setup and the Lorentz method for time-resolved magnetic imaging [39–42]. Our UTEM [schematic in the upper part of Fig. 1(a)] is equipped with both femtosecond and nanosecond pulsed laser systems, which allow us to perform stroboscopic observations on photoinduced ultrafast dynamics at early times with picosecond temporal resolution as well as for a full dynamic cycle with nanosecond temporal resolution. Our key efforts to develop ultrafast Lorentz TEM imaging are summarized as follows: (1) a small ( $\varnothing = 15 \mu\text{m}$ ) LaB<sub>6</sub> photocathode is used to produce pulsed electrons with better transverse coherence, (2) a pulsed laser with shorter wavelengths and higher photon energies are explored to increase the brightness of the pulsed photoelectrons for ultrafast imaging, and (3) removal of beam-limiting apertures in the illumination system also leads to a three times increase in image intensity. Additionally, we employ a focus-ion-beam milling method to prepare thin lamellae

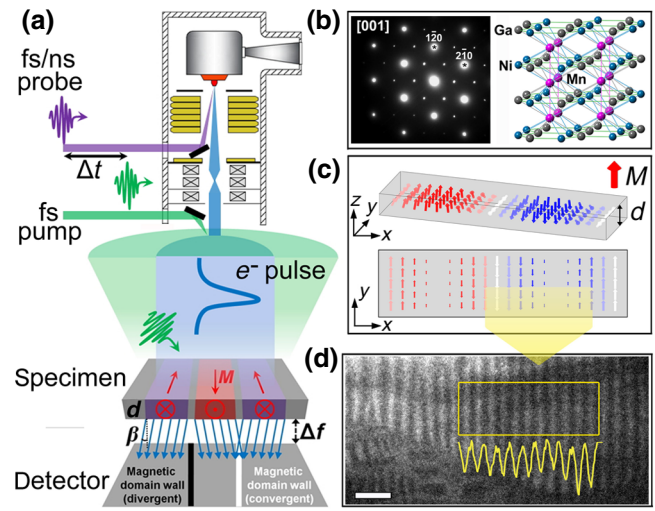


FIG. 1. Schematic representations of UTEM setup and Lorentz magnetic imaging. (a) The pump-probe scheme in UTEM involves the use of a pump laser (central wavelength  $\lambda = 520 \text{ nm}$ , pulse duration  $\delta t = 300 \text{ fs FWHM}$  to initiate photoexcitation and set time zero), and a second probe laser ( $\lambda = 347 \text{ nm}$ ,  $\delta t = 300 \text{ fs}$  for fs-stroboscopic observations or  $\lambda = 355 \text{ nm}$ ,  $\delta t = 10 \text{ ns}$  for ns-stroboscopic observations) to generate electron pulses with varying time delays  $\Delta t$ . In Lorentz imaging, pulsed electrons traverse the magnetic specimen comprised of oppositely magnetized domains with magnetization  $M$  and thickness  $d$ , resulting in bright or dark contrasts at the positions of domain walls. (b) [001]-oriented selected area electron diffraction (SAED) pattern of the Mn-Ni-Ga specimen and its crystallographic model (space group  $P63/mmc$ ). (c) Arrow plot represents a spiral spin texture. (d) Lorentz image of Mn-Ni-Ga with a periodicity of 180 nm by fs-stroboscopic imaging ( $\lambda = 347 \text{ nm}$ ,  $\delta t = 300 \text{ fs}$ , and repetition rate = 50 kHz) at 10-mm over focus with an exposure time of 60 s. An oscillatory line profile is extracted from the rectangle marked region, whose magnitudes depend on the specimen thickness  $d$ , magnetization  $M$ , and defocus value  $\Delta f$ . The magnetic spiral periodicity in the system is 180 nm [the blue or red regions in (c)] which corresponds to one black or white line in (d). Scale bar is 500 nm.

that are welded onto copper bars for mitigating the accumulative heat effects due to repetitive irradiation of laser pulses [43]. Detailed parameters of the microscope and key optical characteristics (central wavelength  $\lambda$ , pulse duration  $\delta t$ , fluence  $F$ , and repetition rate) for the pulsed laser systems and the practical evaluation of spatial resolution of sub-50 nm by pulsed photoelectrons in the Lorentz UTEM are given in Appendix A. A schematic of Fresnel imaging [lower part in Fig. 1(a)] illustrates a simplified ray diagram of magnetic imaging of a thin magnetic slab comprised of oppositely magnetized domains. When traversing a thin specimen of uniform induction  $B$  and of thickness  $d$ , relativistic electrons experience a Lorentz force ( $\vec{F} = -e\vec{v} \times \vec{B}$ ) and are deflected with an angle [ $\beta = e(4\pi B)\lambda d/h$ ] where  $e$  is the electron charge,

the velocity is  $\vec{v}$ , the wave length is  $\lambda$  of relativistic electrons, and Planck's constant is  $h$ . The resultant magnetic contrasts, either excess or deficient electrons at the positions of domain walls, are intimately linked to the in-plane components of induction field  $B$  and the specimen thickness  $d$ , and also depend on the defocus values  $\Delta f$ .

In this study, we use a hexagonal-type Mn-Ni-Ga magnet that has been shown to host skyrmionic spin textures in a wide temperature-field range [38]. Nanosized skyrmions in Mn-Ni-Ga and other chiral magnets are promising candidates as building elements for applications in spintronics and magnetic memory storage [44]. A focus-ion-beam (FIB) milling method is used to prepare a Mn-Ni-Ga lamella, whose morphology and thickness map [45] are shown in Figs. S1 and S2 in the Supplemental Material [43]. Figure 1(b) shows a [001]-oriented electron diffraction pattern of the Mn-Ni-Ga specimen and an atomic model of hexagonal structure (space group  $P63/mmc$ ). For Lorentz UTEM imaging, the specimen temperature is set at 100 K by a liquid-nitrogen-cooled holder and under Lorentz mode. In previous studies, hexagonal Mn-Ni-Ga thin specimens exhibit spiral spin textures with a periodicity of 180 nm as shown in Fig. S3 in the Supplemental Material [43]. Figure 1(c) shows a schematic of magnetic spirals and the corresponding in-plane projection. Accordingly, Fig. 1(d) shows a Lorentz image acquired at 10 mm over focus in fs-stroboscopic imaging ( $\lambda = 347$  nm,  $\delta t = 300$  fs, and repetition rate 50 kHz). The stripelike contrasts extracted from the region marked in Fig. 1(d) are intimately related to in-plane magnetization  $M_{xy}$ , specimen thickness  $d$ , and defocus value  $\Delta f$ . It is noteworthy that the side effect of evanescent near fields generated by the interaction of electrons with a pump photon is negligible in the present study, as discussed in Ref. [36]. Hence, for fixed values of  $\Delta f$  and  $d$ , the changes of intensities in Lorentz images can be associated with the changes in the  $M_{xy}$ .

In order to directly reveal the magnetization dynamics in the Mn-Ni-Ga lamella, we need to assess the changes in Lorentz magnetic contrasts before and after photoexcitation, and select a suitable range of optical fluence for decent ultrafast magnetic signals. Figure 2(a) shows a set of Lorentz images for a selected area in the Mn-Ni-Ga lamella cooled at 100 K, displaying stripelike contrasts that reflect the underlying spiral spin textures [also see Fig. 1(c)]. The time delays ( $t = -50, +50$  ps) are denoted in the images (negative time means image acquisition before the arrival of the pump laser). The size of the pump laser ( $\lambda = 520$  nm,  $\delta t = 300$  fs,  $F = 7 \text{ mJ cm}^{-2}$ , and repetition rate = 50 kHz) at the specimen is measured to be about 100  $\mu\text{m}$  at full-width-half-maximum (FWHM). Prior to ( $-50$  ps) photoexcitation, periodic stripelike contrasts are the prominent features in the Lorentz images. At a 50-ps time delay, the specimen reaches a new thermal equilibrium via electron-phonon scattering. As thermal heating sets the specimen at an elevated temperature above

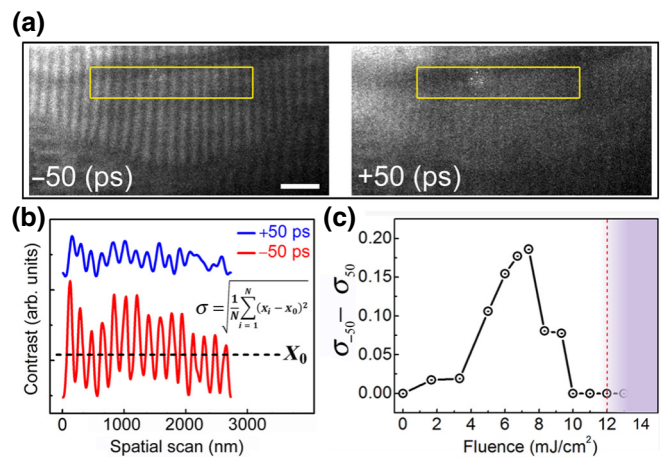


FIG. 2. Lorentz UTEM image of domain wall networks in Mn-Ni-Ga by pulsed photoelectrons. (a) Lorentz images obtained at time delays of  $t = -50$  and  $+50$  ps, for a pump laser ( $\lambda = 520$  nm,  $\delta t = 300$  fs,  $F = 7 \text{ mJ cm}^{-2}$ , and repetition rate = 50 kHz) and a probe laser ( $\lambda = 347$  nm,  $\delta t = 300$  fs, and repetition rate = 50 kHz), and the initial temperature is set at 100 K by a liquid-nitrogen-cooled holder. Exposure time per image is set to 60 s. (b) Normalized line profiles extracted from the rectangle marked in (a), revealing the magnetic contrast evolution before ( $-50$  ps) and after ( $+50$  ps) pump laser. (c) The standard deviation difference  $\sigma_{-50} - \sigma_{+50}$  for line profiles taken at  $-50$  and  $+50$  ps and their pump fluence dependence. Scale bar is 500 nm.

the Curie temperature  $T_C$  (= 350 K) of Mn-Ni-Ga, the stripelike contrasts vanish as a result of thermal demagnetization.

Figure 2(b) shows the normalized line profiles extracted from the rectangle regions marked in Fig. 2(a). In order to quantify the line profiles that reflect the in-plane  $M_{xy}$ , we calculate the standard deviation  $\sigma$  as a measure of  $M_{xy}$ ; in turn, the changes in  $\sigma$  can be calculated as the dynamic parameter to illustrate the rapid changes of magnetic properties [21]. In Fig. 2(c), the values of  $\sigma_{-50 \text{ ps}} - \sigma_{+50 \text{ ps}}$  measured as a function of applied laser fluence reveal that a fluence range between 3.5 and 10  $\text{mJ cm}^{-2}$  is found to give decent ultrafast magnetic responses to photoexcitation, whereas the pump laser fluences below 3.5  $\text{mJ cm}^{-2}$  are too weak and above 10  $\text{mJ cm}^{-2}$  are too intense to generate discernible changes in  $\sigma$ . Importantly, specimen damage can occur for pump fluences over 12  $\text{mJ cm}^{-2}$ .

We first record a set of Lorentz UTEM images for a time span from  $-10$  to  $100$  ps using a pump fluence of  $7 \text{ mJ cm}^{-2}$  (see also Movie 1 in the Supplemental Material [43]). Figure 3(a) shows an array of representative UTEM images with different time delays from which drastic alterations in the stripelike contrasts are clearly observed, demonstrating the photoinduced changes of magnetic structure ( $M_{xy}$ ). Line profiles extracted from the rectangles marked in Fig. 3(a) vividly depict an ultrafast vanishing, then a gradual recurrence, and finally a

complete disappearance of the stripelike contrasts that originate from the magnetic spirals. Figure 3(b) shows the temporal evolution of the normalized standard deviation  $\sigma$  measured from the line profiles in UTEM images in the picosecond time scales, in which three dynamic processes involving four distinct magnetization states are evidently exhibited (as marked “1”: initial magnetization, “2”: ultrafast demagnetization, “3”: partial recovery, “4”: paramagnetic state). Specifically, the first process “1–2” is characterized by a sudden drop of  $\sigma$  at 1.3 ps, and subsequently followed by the second process “2–3” with a rapid rise of  $\sigma$  from 1.3 to 8 ps, and the third process “3–4” with a relatively slow falling of  $\sigma$  from 8 to 40 ps. Since the changes in  $\sigma$  reflect the variations in the  $M_{xy}$ , the measurements in Fig. 3(b) essentially trace the temporal evolution of magnetization of the domain network in the Mn-Ni-Ga lamella. We note that the described magnetic dynamics is reproducible as seen in a second series of UTEM images from a different Mn-Ni-Ga specimen in Appendix A.

The ultrafast demagnetizing process at the magnetic domain level can be unambiguously and reproducibly observed within the time scale of around 1 ps in our measurements. However, the temporal resolution in the present case is about 1 ps, which prevents us from extracting meaningful time constants of the ultrafast demagnetization process as discussed in the study by ultrafast soft x-ray pulse [15]. On the other hand, the time constants for the second process of a partial magnetization recovery and the third process of a thermally driven demagnetization can be well estimated by fitting the measured  $\sigma$  with empirical exponential functions, yielding  $\tau_{2-3} = 3 \pm 0.5$  ps and  $\tau_{3-4} = 12 \pm 1$  ps, respectively. These dynamic processes as observed in Mn-Ni-Ga by UTEM reveal a general dynamic nature for demagnetization and relevant ultrafast evolution in magnetic metals as discussed in previous literature [1,8,9]. It is worth highlighting that our high spatiotemporal view of ultrafast magnetization dynamics in the complex nanoscale domain networks in Mn-Ni-Ga lamella is now augmented with a real-space magnetic imaging capability with sub-50-nanometer resolution.

The fundamental ultrafast behavior in metal magnets can be described by a phenomenological model accounting for the intricate interplay between the electron, spin, and lattice subsystems [1,8]. Upon photoexcitation, the electrons almost instantaneously acquire photonic energies within tens of femtoseconds and the hot electrons rapidly transfer their excess energies to the spins within hundreds of femtoseconds, resulting in an ultrafast destruction of spin angular momentum [the first process “1–2” in Fig. 3(b)]. As the electron-spin subsystem thermalizes the lattices in the picosecond timescale, a partial recovery of magnetization occurs [the second process “2–3” in Fig. 3(b)]. Further thermalization in the electron-spin-lattice subsystems reaches a new thermally equilibrated state at an elevated temperature, at which the

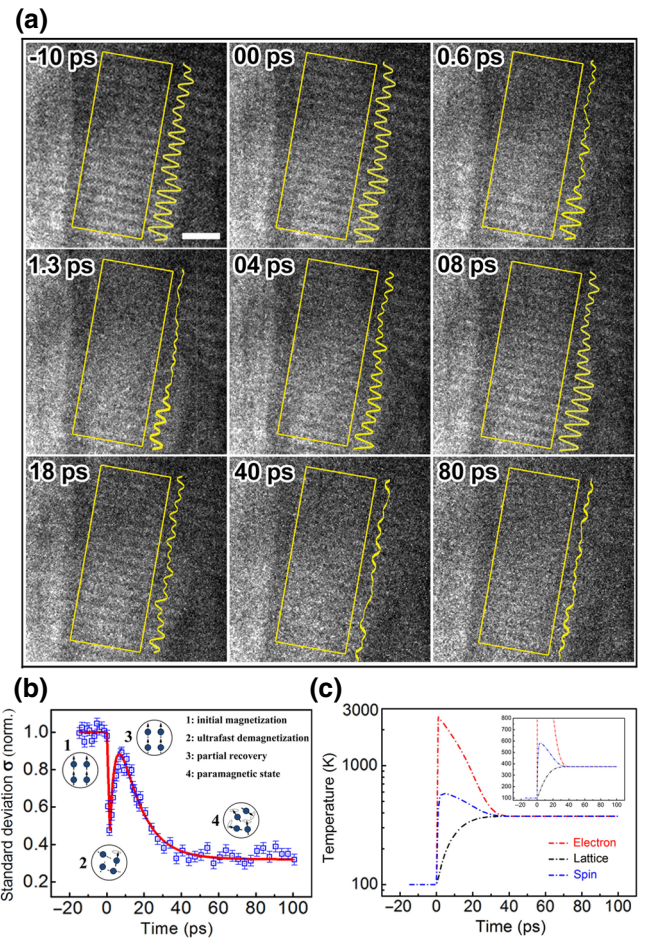


FIG. 3. Ultrafast magnetization dynamics in Mn-Ni-Ga with a nanometer-picosecond spatiotemporal resolution. (a) Temporal snapshots of Lorentz images captured at different time delays as indicated and under the following conditions: pump laser ( $\lambda = 520$  nm,  $\delta t = 300$  fs,  $F = 7$  mJ cm $^{-2}$ , and repetition rate = 50 kHz), probe laser ( $\lambda = 347$  nm,  $\delta t = 300$  fs, and repetition rate = 50 kHz), the initial temperature is 100 K, exposure time per snapshot of 15 s. Line profiles extracted from the yellow rectangle marked regions are overlaid. (b) Calculated standard deviation  $\sigma$  of line profiles for a whole set of time series. Four distinct magnetic states are indicated and their respective atomic spin models are illustrated. The time constants of the second process “2–3” and the third process “3–4” can be estimated by fitting the  $\sigma$  with empirical double-exponential functions, yielding  $\tau_{2-3} = 3 \pm 0.5$  ps and  $\tau_{3-4} = 12 \pm 1$  ps, respectively. (c) Simulations of temporal evolution of temperatures for the electron, the spin, and the lattice subsystems with the three-temperature model. Scale bar is 500 nm.

magnetization is suppressed or even destroyed above  $T_C$  [the third process “3–4” in Fig. 3(b)]. In order to analyze the magnetic changes upon the fs laser excitation, we also calculate the electron system temperature  $T_e$ , spin system temperature  $T_s$ , and lattice system temperature  $T_l$  by the coupled differential equations[1], and the longitudinal

temperature gradients (normal to surface) and the exponential decay of the source within the material are taken into account [46]. The three-temperature model (3TM) equations read

$$C_e(T_e) \frac{\partial T_e}{\partial t} = \frac{\partial}{\partial x} \left( k_e(T_e, T_l) \frac{\partial T_e}{\partial x} \right) - G_{el}(T_e - T_l) - G_{es}(T_e - T_s) + Q(x, t),$$

$$C_s(T_s) \frac{\partial T_s}{\partial t} = -G_{es}(T_s - T_e) - G_{sl}(T_s - T_l),$$

$$C_l(T_l) \frac{\partial T_l}{\partial t} = -G_{el}(T_l - T_e) - G_{sl}(T_l - T_s),$$

$$Q(x, t) = 0.94 \frac{(1-R)}{\delta t} F \exp \left[ -\frac{x}{d} - 2.77 \left( \frac{t}{\delta t} \right)^2 \right].$$

where  $C_l$ ,  $C_e$ , and  $C_s$  are the respective specific heats for the lattice, electron, and spin subsystems, and the electronic specific heat  $C_e(T_e) = \gamma T_e$ , which is approximated linearly with electron temperature  $T_e$ .  $G_{el}$ ,  $G_{es}$ , and  $G_{sl}$  are the respective interaction constants for electron-lattice, electron-spin, and spin-lattice,  $k_e$  is the thermal conductivity of the electrons, and  $x$  is the direction normal to the surface [47,48].  $Q(x, t)$  is the laser source term that has an exponential decay in space to account for absorption in a nontransparent medium, with parameters of reflectivity  $R$ , penetration depth  $d$ , fluence  $F$ , and pulse duration  $\delta t$ . The temporal evolution of temperatures about these three subsystems and the corresponding magnetization dynamics are shown in the Figs. 3(b) and 3(c). Importantly, the electron and spin temperatures can quickly rise after the photoexcitation, resulting in a rapid destruction of magnetic order and the immediate alteration of magnetic domains. However, the phenomenological model does not capture the underlying complex angular momentum and energy transfers among the electron-spin-lattice subsystems [2,49,50]. Microscopic understanding on the exact channels of energy and momentum transfers in magnetic metals is still an open question. In the present case, the domain network may offer an additional extrinsic mechanism for ultrafast demagnetization by direct spin transfer across the domain walls via “hot electron” transport [27]. It is worth noting that locally the temporal changes in magnetic contrasts are varied from areas to areas in Fig. 3(b), which could be associated with the local variations in structure or composition at the nanoscale. Such inhomogeneity in magnetic dynamics observed in Ni also provides evidence of the possible presence of coexisting phases during the ultrafast demagnetization process [51]. Direct imaging of magnetic dynamics with high spatiotemporal resolution may provide a unique tool for elucidating the proposed direct spin transfer mechanism [27], and

revealing the local inhomogeneity of transient states during photoinduced magnetic phase transitions [51].

Finally, using the ns-stroboscopic imaging ( $\lambda = 355$  nm,  $\delta t = 10$  ns, and repetition rate = 10 kHz) we can obtain a full cycle of magnetization dynamics in Mn-Ni-Ga (see Movie 2 in the Supplemental Material [43]) initiated by a single femtosecond pump laser pulse ( $\lambda = 520$  nm,  $\delta t = 300$  fs,  $F = 7$  mJ cm<sup>-2</sup>, and repetition rate = 10 kHz). Figure 4(a) presents the representative snapshots taken at different time delays, displaying a gradual recovery of the stripelike contrasts as the specimen thermalizes to its initial state in the microsecond timescale. In Fig. 4(b), the line profiles extracted from the regions marked in Fig. 4(a) reveal a temporal evolution of the domain networks. A rapid suppression of magnetic spiral contrasts at  $t = 0.367$   $\mu$ s can be attributed to a thermally driven demagnetization above  $T_C$  [the paramagnetic state “4” as also seen in Fig. 3(a)]. Subsequently, the temperature of the specimen decreases following by heat dissipation to the supporting copper bars resulting in nucleation, growth, and rearrangement of domain networks, the temperature change for the specimen has been theoretically calculated with a two-dimensional heat diffusion model in Appendix B. Importantly, the magnetic domain structures in Mn-Ni-Ga fully recover to the initial state, as evidenced in the nearly perfect match of line profiles taken at  $t = 21.437$   $\mu$ s and at  $t = 0$   $\mu$ s [Fig. 4(b)].

In order to extract the time constant  $\tau_{th}$  for the heat dissipation process, we fit the time-dependent standard deviations  $\sigma$  [Fig. 4(c)] with an exponential function to yield a  $\tau_{th} = 6.9 \pm 0.8$   $\mu$ s. It is noteworthy that additional bend contours (marked by white arrows) are present in Fig. 4(a) due to microstructure distortion following thermo diffusion, and certain related dynamic behaviors are also shown in the Supplemental Material Fig. S4 [43]. Moreover, we can also attribute this structural feature to nanomechanical oscillations as recently discussed by Flannigan and coworkers [52–54]. It is notable in our experiments that the dynamic features of magnetic domains (walls) via line profiles are not affected visibly by the presence of the bend contours. This fact demonstrates that the ultrafast dynamic properties of magnetic domain networks can be essentially characterized by Lorentz UTEM images as mentioned in above.

In recent years, the phenomenon of ultrafast demagnetization and relevant magnetic transient states resulting from excitation by an intense femtosecond laser pulse has been extensively investigated, and the underlying mechanism remains a hotly debated issue. Our investigations on dynamic features for the magnetic domain networks of Mn-Ni-Ga lamella reveal a rich variety of phenomena subsequent to femtosecond laser excitations, in accordance with a general trend of ultrafast magnetization dynamics as reported for magnetic metals [1,8,9]. In comparison with either time-resolved optics or x-rays

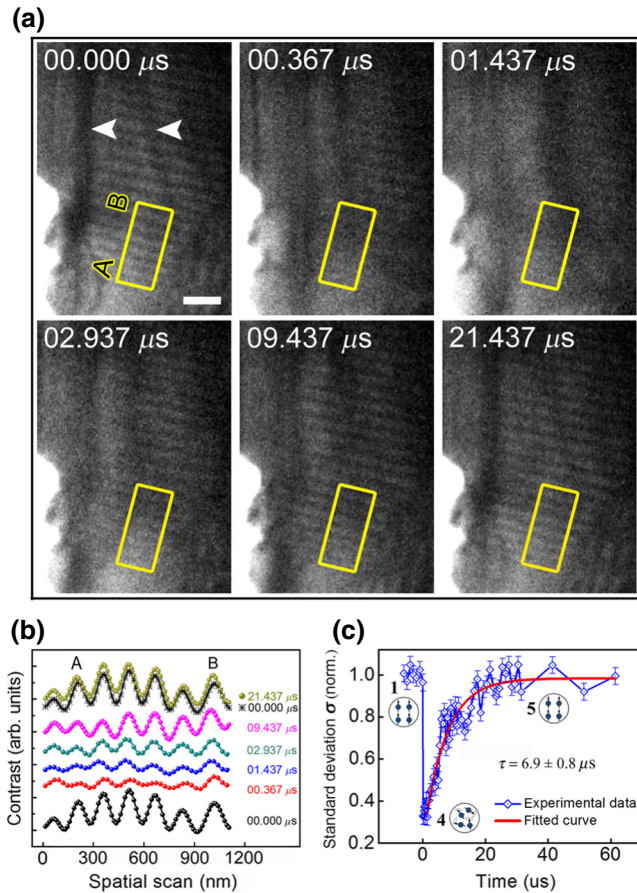


FIG. 4. A full cycle of magnetization dynamics in Mn-Ni-Ga with a nanometer-nanosecond spatiotemporal resolution. (a) Temporal snapshots of Lorentz images captured at different time delays as indicated and under the following conditions: pump laser ( $\lambda = 520$  nm,  $\delta t = 300$  fs,  $F = 7$  mJ cm $^{-2}$ , and repetition rate = 10 kHz), probe laser ( $\lambda = 355$  nm,  $\delta t = 10$  ns, and repetition rate = 10 kHz), the initial temperature is 100 K, exposure time per snapshot of 3 s. The white arrows indicate additional bend contours, which do not affect the analyses of magnetic contrast. See the text for details. (b) Line profiles extracted from the yellow rectangle marked regions in (a). Note that the nearly perfect reproduced line profiles  $t = 21.437$   $\mu$ s and  $t = 0$   $\mu$ s suggest that the magnetic spirals fully recover to the initial state. (c) Temporal evolution of the standard deviation  $\sigma$  of the magnetic contrast line profiles, showing the complete recovery of the magnetization as the electron-spin-lattice subsystems cool down and the heat transfers to the supports. The time constant of the fourth process “4–5” can be estimated by fitting the  $\sigma$  with a single exponential function, yielding  $\tau_{\text{th}} = 6.9 \pm 0.8$   $\mu$ s. Scale bar is 500 nm.

microscopy ultrafast techniques [10,16,19,21], one outstanding strength of the Lorentz UTEM approach for studying magnetization dynamics lies in its real-space imaging of magnetic structures with nanometer resolution. Such a high spatiotemporal resolution is ideally suited to elucidate a possible ultrafast demagnetization

mechanism involving spin-transport processes in nonuniform magnetization (domain walls or noncollinear spin textures). The Lorentz UTEM also provides a nanometer-nanosecond-resolved magnetic imaging for recording a full cycle of magnetization dynamics. From a dynamic cycle, one can determine a proper repetition rate for a stroboscopic observation and can also obtain the nature for thermally driven magnetic phase transitions. Such a real-space Lorentz imaging with nanometer-nanosecond resolution provides an ideal tool for observation of fast magnetization switching launched by acoustic waves [55].

### III. CONCLUSION

In summary, by maximizing the collection efficiency of photoelectrons for imaging and interfacing an ultrafast transmission electron microscope with a fs-ns laser system, we explore the time-resolved (both picosecond and nanosecond) capability of Lorentz TEM for a real-space imaging of ultrafast magnetization dynamics initiated by laser pulses. Using fs-laser-generated photoelectrons, we demonstrate a picosecond view of ultrafast magnetization dynamics of magnetic spirals in a Mn-Ni-Ga specimen with a sub-50-nm spatial resolution. Our Lorentz UTEM observations reveal three successive dynamic processes of magnetization transitions involving four distinct magnetic states, namely, upon optical excitation, the Mn-Ni-Ga first undergoes an ultrafast optical demagnetization around 1 ps, then a rapid recovery of magnetization within a few picoseconds, and finally a thermally driven demagnetization toward a paramagnetic state in tens of picoseconds. Moreover, using ns-laser-generated photoelectrons, we record a full cycle of magnetization

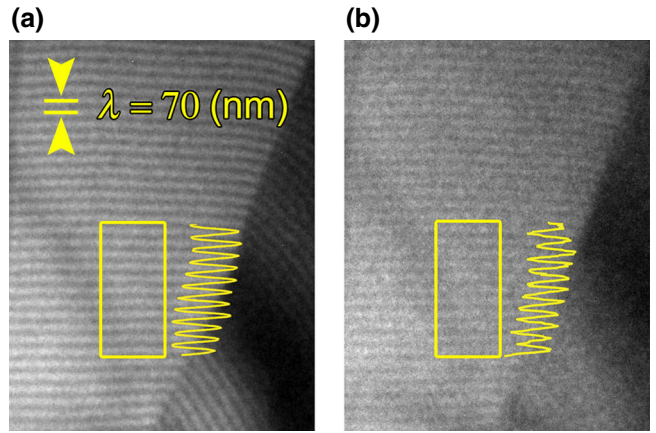


FIG. 5. Evaluation of spatial resolution for Lorentz UTEM. Lorentz images of 70-nm spirals in FeGe lamella taken at a defocus value of 5 mm and at 230 K. (a) Lorentz image by continuous thermionic electrons. (b) Lorentz image by pulsed photoelectrons. The pulsed laser for photoelectrons is characterized by a central wavelength  $\lambda = 347$  nm, duration  $\delta t = 300$  fs, and repetition rate = 50 kHz.

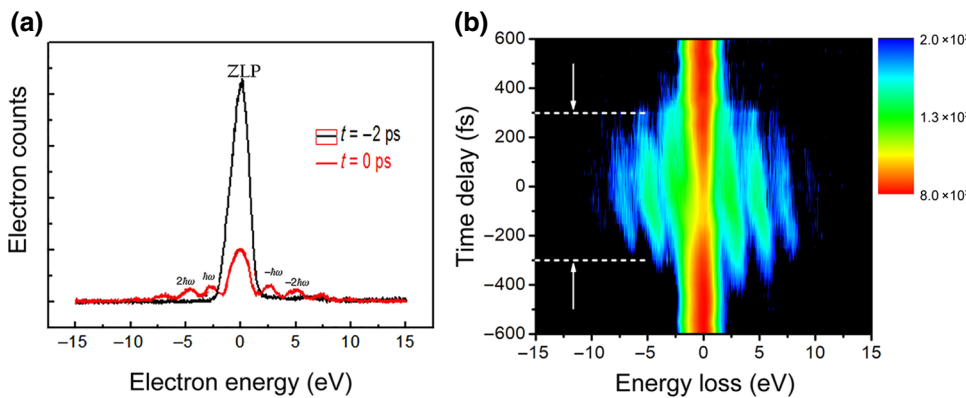


FIG. 6. Temporal pulse characterization. Electron energy-loss spectra taken from carbon nanotubes at different delay times. (a) Electron energy-loss spectra show the electron–photon interaction, modifying the electron energy in steps of  $\pm \hbar\omega$ . (b) Electron energy-loss spectra as a function of delay time for the temporal characterization of employed electron pulses. Arrows: extracted electron pulse duration of approximately 600 fs.

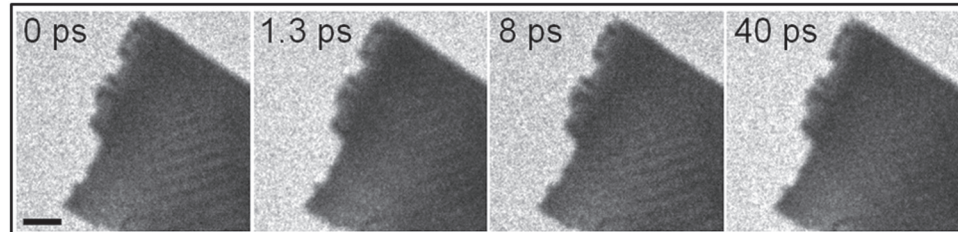
dynamics in Mn-Ni-Ga subsequent to photoexcitation in a time span of tens of microseconds. Based on the three-temperature approximation, we briefly analyze the temporal evolution of the lattice, the electrons, and the spin subsystems, and the relevant thermodynamic transitions following the electron-lattice thermalization are also discussed. Our results clearly demonstrate that real-space magnetic imaging with high spatiotemporal resolution is highly desirable for the study of magnetic dynamics and magnetization phase transition in complex nanoscale spin textures.

#### ACKNOWLEDGMENTS

We acknowledge the support for sample preparation from Haifeng Du and the insightful discussion with Michael Farle and Wei He.

This work was financially supported by the National Key Research and Development Program of China (Grants No. 2016YFA0300303, No. 2017YFA0504703, and No. 2017YFA0302904), the National Basic Research Program of China (Grant No. 2015CB921304), the National Natural Science Foundation of China (Grants No. 11774391, No. 11774403, and No. 11804381), the Strategic Priority Research Program (B) of the Chinese Academy of Sciences (Grants No. XDB25000000 and No. XDB07020000), the Scientific Instrument Developing Project of the Chinese Academy of Sciences (Grant No. ZDKYYQ20170002), and the Start-up fund from SUSTech (Grant No. Y01236237).

Authors M. Z. and Z.-A. L. contributed equally to this work.



#### APPENDIX A: UTEM SETUP AND PUMP–PROBE SCHEME

Ultrafast pump-probe experiments are performed in our home-built UTEM modified from a JEOL-2000EX microscope operating at 160 kV. For pumping, frequency-doubled (Spirit, Spectra-Physics) laser pulses are used (central wavelength  $\lambda = 520$  nm, pulse duration  $\delta t = 300$  fs at FWHM) with variable fluence  $F$  up to  $15 \text{ mJ cm}^{-2}$ . The size of the pump laser at the specimen position is estimated to be  $100 \mu\text{m}$  (FWHM), providing a uniform laser excitation, as also confirmed in the *ex-situ* measurements by a beam profiler (BeamOn HR, Duma Optronics). For probing by electron pulses, a LaB<sub>6</sub> photocathode ( $\varnothing = 15 \mu\text{m}$ ) is driven, respectively, by frequency-threecold fs laser pulses ( $\lambda = 347$  nm,  $\delta t = 300$  fs) or ns laser pulses (Stele-A-1, ZY LASER,  $\lambda = 355$  nm,  $\delta t = 10$  ns) at different repetition rates. Note that we use shorter wavelengths and higher photon energies of the fs laser ( $\lambda = 347$  nm,  $h\nu = 3.57$  eV) and ns laser ( $\lambda = 355$  nm,  $h\nu = 3.49$  eV) for efficient generation of pulsed photoelectrons from the LaB<sub>6</sub> cathode with a work function in the range of 2.5–2.8 eV depending on its facets and working conditions. The 50-kHz repetition rate is used for the fs-stroboscopic imaging to generate pulsed photoelectrons. The pulsed electrons arriving at the CCD camera detector are directly measured to be approximately 100 electrons per pulse. The time delay for pump-probe measurements is set by a mechanically motorized delay stage (Newport M-ILS250CC). For the ns-stroboscopic imaging, we use a 10-kHz repetition rate, resulting in approximately  $5 \times 10^4$  electrons per pulse, and the pump-probe time delay is set by a digital delay generator (SRS DG645).

FIG. 7. Reproducibility of experimental observation. A second series of UTEM images from a different Mn-Ni-Ga specimen in which we observed the same evolution as seen in Fig. 3. Scale bar is 500 nm.

In the Lorentz UTEM experiments, a 300- $\mu\text{m}$  condenser aperture is used for taking the time-resolved images of magnetic domains with a good signal-to-noise ratio. A sub-50-nm spatial resolution for domain structures is demonstrated as shown in Fig. 5. A double-tilt liquid-nitrogen-cooled holder is used to perform the UTEM observations at 100 K. Images are recorded by a CCD camera (Gatan Orius SC200) with exposure times of 15 s per image for fs-stroboscopic imaging and 3 s per image for ns-stroboscopic imaging. All Fresnel images are recorded at a defocus value of approximately 10 mm with the objective

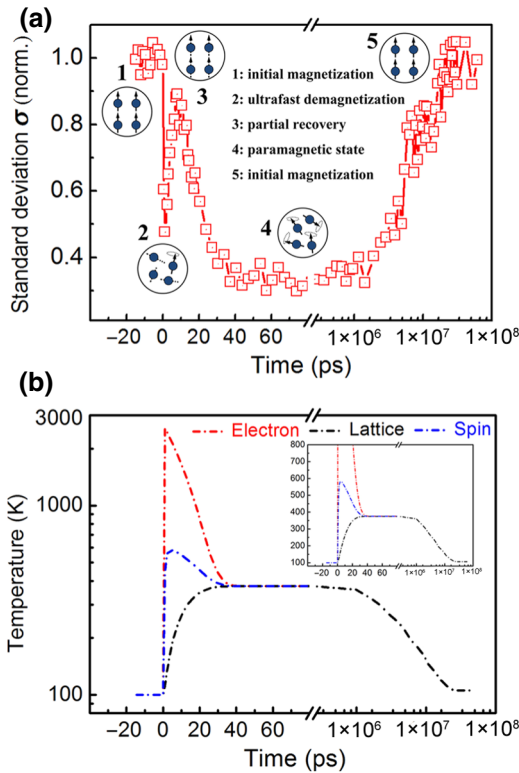


FIG. 8. Evolution of magnetic domain walls and three-temperature model simulation for a reversible cycle with a pump fluence of 7 mJ/cm<sup>2</sup>. (a) The experimental data display four times of magnetization switching by an ultrafast laser pulse from picosecond to microsecond timescales, and ensure the dynamics of the domain wall is reversible for stroboscopic observation. Five distinct magnetic states are indicated and their respective atomic spin models are illustrated. (b) Simulations of temperatures for the electron, the spin, and the lattice subsystems. The temperature of electrons rises instantaneously and then the hot electrons transfer their excess energies to the spins rapidly, resulting in an ultrafast demagnetization [the process “1–2” in (a)]. As the electron-spin subsystem thermalizes the lattices in the picosecond timescale, a partial recovery of magnetization occurs [the process “2–3” in (a)]. Further thermalization in the electron-spin-lattice subsystems reaches a new thermally equilibrated state at an elevated temperature above  $T_C$  [the process “3–4” in (a)]. Finally, the specimen cools down via heat dissipation to the supporting copper bars [the process “4–5” in (a)].

lens switched off (i.e., Lorentz mode with residual magnetic field of approximately 100 Oe).

For synchronizing the pump laser and pulsed electrons and for characterizing the temporal resolution, we make use of the electron-optical cross-correlation in laser-induced near fields [37]. At delay times for which the optical pump pulse and electron-probe pulses overlap at the sample surface, the electron energy spectra exhibit sidebands separated by the photon energy, as shown in Fig. 6. The 600-fs duration of the electron pulses can be extracted from the temporal width of the highest-order photon sidebands when the microscope is operated at a single electron per pulse regime. However, we note that for the present study of direct magnetic imaging, the microscope is operated at multielectrons per pulse regime and the time resolution of the UTEM is estimated to be around 1 ps due to the space charge effects [41,42].

From experimental sides, we verify that our observations are repeated for the same area and reproducible for different areas of the specimen. We provide a second series of UTEM images from a different Mn-Ni-Ga specimen, as shown in Fig. 7.

## APPENDIX B: DATA ANALYSIS AND SIMULATIONS

As the stripelike contrasts in the Lorentz images originate from the domain networks in Mn-Ni-Ga, in order to exhibit the changes in the in-plane magnetization  $M_{xy}$ , we can measure the variations in standard deviation  $\sigma$  of line profiles using  $\sigma = [\sum(X_i - X_0)^2/N]^{1/2}$  [21], where  $X_0$  is the average value of the contrast  $X_i$ , and  $N$  is the pixel number of the line profile.

To theoretically analyze the dynamic evolutions of a magnetic structure as observed in our experiments, two models are used to investigate the specific features of transient states. We first use the three-temperature model for the sub-100-ps dynamics as described by Beaurepaire [1], calculating the light-induced temperatures  $T$  of the electron, spin, and lattice. In addition, the longitudinal temperature gradients (normal to surface) and the exponential decay of the source within the material are taken into account for a more accurate simulation. The thermal constants are estimated from Ref. [48], the interaction constants are estimated from Ref. [47], and the laser source term is calculated by our pump laser characteristics. On the longer time scales, we solve the two-dimensional heat diffusion equation and calculate the temperature of the sample with COMSOL Multiphysics™. The evolution of magnetic domain walls and the estimated temperature in a full cycle are shown in Fig. 8. The realistic optical and thermal parameters for simulations are listed in Table I.

TABLE I. The realistic optical and thermal parameters for simulations.

$C_e = \gamma T_e$	$C_l^b$	$C_s^b$	$G_{el}^c$	$G_{es}^c$	$G_{sl}^c$
$\gamma = 540^a$	2.7	0.22	0.27	0.1	1

<sup>a</sup>J m<sup>-3</sup> K<sup>-2</sup>

<sup>b</sup>10<sup>6</sup> J m<sup>-3</sup> K<sup>-1</sup>

<sup>c</sup>10<sup>16</sup> W m<sup>-3</sup> K<sup>-1</sup>

- [1] E. Beaurepaire, J. C. Merle, A. Daunois, and J. Y. Bigot, Ultrafast Spin Dynamics in Ferromagnetic Nickel, *Phys. Rev. Lett.* **76**, 4250 (1996).
- [2] G. P. Zhang and W. Hubner, Laser-Induced Ultrafast Demagnetization in Ferromagnetic Metals, *Phys. Rev. Lett.* **85**, 3025 (2000).
- [3] M. van Kampen, C. Jozsa, J. T. Kohlhepp, P. LeClair, L. Lagae, W. J. M. de Jonge, and B. Koopmans, All-Optical Probe of Coherent Spin Waves, *Phys. Rev. Lett.* **88**, 227201 (2002).
- [4] G. P. Ju, J. Hohlfeld, B. Bergman, R. J. M. van de Veerdonk, O. N. Mryasov, J. Y. Kim, X. W. Wu, D. Weller, and B. Koopmans, Ultrafast Generation of Ferromagnetic Order via a Laser-Induced Phase Transformation in FeRh Thin Films, *Phys. Rev. Lett.* **93**, 197403 (2004).
- [5] A. V. Kimel, A. Kirilyuk, A. Tsvetkov, R. V. Pisarev, and T. Rasing, Laser-induced ultrafast spin reorientation in the antiferromagnet TmFeO<sub>3</sub>, *Nature* **429**, 850 (2004).
- [6] B. Koopmans, G. Malinowski, F. D. Longa, D. Steiauf, M. Faehnle, T. Roth, M. Cinchetti, and M. Aeschlimann, Explaining the paradoxical diversity of ultrafast laser-induced demagnetization, *Nat. Mater.* **9**, 259 (2010).
- [7] J. Y. Bigot, M. Vomir, and E. Beaurepaire, Coherent ultrafast magnetism induced by femtosecond laser pulses, *Nat. Phys.* **5**, 515 (2009).
- [8] A. Kirilyuk, A. V. Kimel, and T. Rasing, Ultrafast optical manipulation of magnetic order, *Rev. Mod. Phys.* **82**, 2731 (2010).
- [9] B. Koopmans, M. van Kampen, J. T. Kohlhepp, and W. J. M. de Jonge, Ultrafast Magneto-Optics in Nickel: Magnetism or Optics?, *Phys. Rev. Lett.* **85**, 844 (2000).
- [10] C. Boeglin, E. Beaurepaire, V. Halte, V. Lopez-Flores, C. Stamm, N. Pontius, H. A. Durr, and J. Y. Bigot, Distinguishing the ultrafast dynamics of spin and orbital moments in solids, *Nature* **465**, 458 (2010).
- [11] A. Eschenlohr, M. Battiatto, P. Maldonado, N. Pontius, T. Kachel, K. Holldack, R. Mitzner, A. Föhlsch, P. M. Oppeneer, and C. Stamm, Ultrafast spin transport as key to femtosecond demagnetization, *Nat. Mater.* **12**, 332 (2013).
- [12] G. M. Muller, G. Eilers, Z. Wang, M. Scherff, R. Ji, K. Nielsch, C. A. Ross, and M. Munzenberg, Magnetization dynamics in optically excited nanostructured nickel films, *New J. Phys.* **10**, 123004 (2008).
- [13] C. D. Stanciu, F. Hansteen, A. V. Kimel, A. Kirilyuk, A. Tsukamoto, A. Itoh, and T. Rasing, All-Optical Magnetic Recording with Circularly Polarized Light, *Phys. Rev. Lett.* **99**, 047601 (2007).
- [14] C. H. Lambert, S. Mangin, B. S. D. Ch. S. Varaprasad, Y. K. Takahashi, M. Hehn, M. Cinchetti, G. Malinowski, K. Hono, Y. Fainman, M. Aeschlimann, and E. E. Fullerton, All-optical control of ferromagnetic thin films and nanostructures, *Science* **345**, 1337 (2014).
- [15] C. Dornes, *et al.*, The ultrafast Einstein-de Haas effect, *Nature* **565**, 209 (2019).
- [16] G. P. Zhang, W. Hubner, G. Lefkidis, Y. H. Bai, and T. F. George, Paradigm of the time-resolved magneto-optical Kerr effect for femtosecond magnetism, *Nat. Phys.* **5**, 499 (2009).
- [17] D. J. Hilton, R. P. Prasankumar, S. A. Trugman, A. J. Taylor, and R. D. Averitt, On photo-induced phenomena in complex materials: Probing quasiparticle dynamics using infrared and far-infrared pulses, *J. Phys. Soc. Jpn.* **75**, 011006 (2006).
- [18] T. Kampfrath, A. Sell, G. Klatt, A. Pashkin, S. Mährlein, T. Dekorsy, M. Wolf, M. Fiebig, A. Leitenstorfer, and R. Huber, Coherent terahertz control of antiferromagnetic spin waves, *Nat. Photonics* **5**, 31 (2011).
- [19] C. Stamm, T. Kachel, N. Pontius, R. Mitzner, T. Quast, K. Holldack, S. Khan, C. Lupulescu, E. F. Aziz, M. Wietstruk, H. A. Dür, and W. Eberhardt, Femtosecond modification of electron localization and transfer of angular momentum in nickel, *Nat. Mater.* **6**, 740 (2007).
- [20] B. Pfau, *et al.*, Ultrafast optical demagnetization manipulates nanoscale spin structure in domain walls, *Nat. Commun.* **3**, 1100 (2012).
- [21] C. V. Schmising, B. Pfau, M. Schneider, C.M. Günther, M. Giovannella, J. Perron, B. Vodungbo, L. Müller, F. Capotondi, E. Pedersoli, N. Mahne, J. Lüning, and S. Eisebitt, Imaging Ultrafast Demagnetization Dynamics after a Spatially Localized Optical Excitation, *Phys. Rev. Lett.* **112**, 217203 (2014).
- [22] C. Spezzani, *et al.*, Magnetization and Microstructure Dynamics in Fe/MnAs/GaAs(001): Fe Magnetization Reversal by a Femtosecond Laser Pulse, *Phys. Rev. Lett.* **113**, 247202 (2014).
- [23] O. Kfir, S. Zayko, C. Nolte, M. Sivis, M. Möller, B. Hebler, S. S. P. K. Arekapudi, D. Steil, S. Schäfer, M. Albrecht, O. Cohen, S. Mathias, and C. Ropers, Nanoscale magnetic imaging using circularly polarized high-harmonic radiation, *Sci. Adv.* **3**, eaao4641 (2017).
- [24] B. C. Choi, M. Belov, W. K. Hiebert, G. E. Ballentine, and M. R. Freeman, Ultrafast Magnetization Reversal Dynamics Investigated by Time Domain Imaging, *Phys. Rev. Lett.* **86**, 728 (2001).
- [25] B. Barwick, D. J. Flannigan, and A. H. Zewail, Photon-induced near-field electron microscopy, *Nature* **462**, 902 (2009).
- [26] P. Fischer, D. H. Kim, W. L. Chao, J. A. Liddle, E. H. Anderson, and D. T. Attwood, Soft X-ray microscopy of nanomagnetism, *Mater. Today* **9**, 26 (2006).
- [27] B. Vodungbo, J. Gautier, G. Lambert, A. B. Sardinha, M. Lozano, S. Sebban, M. Ducouso, W. Boutu, K. Li, B. Tudu, M. Tortarolo, R. Hawaldar, R. Delaunay, V. López-Flores, J. Arabski, C. Boeglin, H. Merdji, P. Zeitoun, and J. Lüning, Laser-induced ultrafast demagnetization in the presence of a nanoscale magnetic domain network, *Nat. Commun.* **3**, 999 (2012).

- [28] T. Eggebrecht, M. Möller, J. G. Gatzmann, N. R. da Silva, A. Feist, U. Martens, H. Ulrichs, M. Münzenberg, C. Ropers, and S. Schäfer, Light-Induced Metastable Magnetic Texture Uncovered by *in situ* Lorentz Microscopy, *Phys. Rev. Lett.* **118**, 097203 (2017).
- [29] K. Harada, O. Kamimura, H. Kasai, T. Matsuda, A. Tonomura, and V. V. Moshchalkov, Direct observation of vortex dynamics in superconducting films with regular arrays of defects, *Science* **274**, 1167 (1996).
- [30] X. W. Fu, S. D. Pollard, B. Chen, B. K. Yoo, H. Yang, and Y. M. Zhu, Optical manipulation of magnetic vortices visualized *in situ* by Lorentz electron microscopy, *Sci. Adv.* **4**, eaat3077 (2018).
- [31] K. Ura, H. Fujioka, and T. Hosokawa, Picosecond pulse stroboscopic scanning electron-microscope, *J. Electron Microsc.* **27**, 247 (1978).
- [32] K. Ura, H. Fujioka, T. Saito, and N. Morimura, Development of microsecond pulse stroboscopic TEM - Mark-I, *J. Electron Microsc.* **27**, 311 (1978).
- [33] H. S. Park, J. S. Baskin, and A. H. Zewail, 4D lorentz electron microscopy imaging: Magnetic domain wall nucleation, reversal, and wave velocity, *Nano Lett.* **10**, 3796 (2010).
- [34] K. B. Schliep, P. Quartermann, J. P. Wang, and D. J. Flannigan, Picosecond Fresnel transmission electron microscopy, *Appl. Phys. Lett.* **110**, 222404 (2017).
- [35] G. Berruto, I. Madan, Y. Murooka, G. M. Vanacore, E. Pomarico, J. Rajeswari, R. Lamb, P. Huang, A. J. Kruchkov, Y. Togawa, T. LaGrange, D. McGruther, H. M. Rønnow, and F. Carbone, Laser-Induced Skyrmion Writing and Erasing in an Ultrafast Cryo-Lorentz Transmission Electron Microscope, *Phys. Rev. Lett.* **120**, 117201 (2018).
- [36] N. Rubiano da Silva, M. Möller, A. Feist, H. Ulrichs, C. Ropers, and S. Schäfer, Nanoscale Mapping of Ultrafast Magnetization Dynamics with Femtosecond Lorentz Microscopy, *Phys. Rev. X* **8**, 031052 (2018).
- [37] A. Feist, N. Bach, N. Rubiano da Silva, T. Danz, M. Möller, K. E. Priebe, T. Domröse, J. G. Gatzmann, S. Rost, J. Schauss, S. Strauch, R. Bormann, M. Sivis, S. Schäfer, and Claus Ropers, Ultrafast transmission electron microscopy using a laser-driven field emitter: Femtosecond resolution with a high coherence electron beam, *Ultramicroscopy* **176**, 63 (2017).
- [38] W. H. Wang, Y. Zhang, G. Z. Xu, L. C. Peng, B. Ding, Y. Wang, Z. P. Hou, X. M. Zhang, X. Y. Li, E. K. Liu, S. G. Wang, J. W. Cai, F. W. Wang, J. Q. Li, F. X. Hu, G. H. Wu, B. G. Shen, and X.-X. Zhang, A centrosymmetric hexagonal magnet with superstable biskyrmion magnetic nanodomains in a wide temperature range of 100–340 K, *Adv. Mater.* **28**, 6887 (2016).
- [39] G. L. Cao, S. S. Sun, Z. W. Li, H. F. Tian, H. X. Yang, and J. Q. Li, Clocking the anisotropic lattice dynamics of multi-walled carbon nanotubes by four-dimensional ultrafast transmission electron microscopy, *Sci. Rep.* **5**, 8404 (2015).
- [40] S. S. Sun, L. L. Wei, Z. W. Li, G. L. Cao, Y. Liu, W. J. Lu, Y. P. Sun, H. F. Tian, H. X. Yang, and J. Q. Li, Direct observation of an optically induced charge density wave transition in 1T-TaSe<sub>2</sub>, *Phys. Rev. B* **92**, 224303 (2015).
- [41] M. Zhang, G. L. Cao, H. F. Tian, S. S. Sun, Z. W. Li, X. Y. Li, C. Guo, Z. A. Li, H. X. Yang, and J. Q. Li, Picosecond view of a martensitic transition and nucleation in the shape memory alloy Mn<sub>50</sub>Ni<sub>40</sub>Sn<sub>10</sub> by four-dimensional transmission electron microscopy, *Phys. Rev. B* **96**, 174203 (2017).
- [42] S. S. Sun, Z. W. Li, Z. A. Li, R. J. Xiao, M. Zhang, H. F. Tian, H. X. Yang, and J. Q. Li, Cooperative inter- and intra-layer lattice dynamics of photoexcited multi-walled carbon nanotubes studied by ultrafast electron diffraction, *Nanoscale* **10**, 7465 (2018).
- [43] See Supplemental Material <http://link.aps.org/supplemental/10.1103/PhysRevApplied.12.034037> for detailed descriptions of the sample preparation, measurement of specimen thickness, and the evolution of bend contours in Mn-Ni-Ga launched by femtosecond laser pulses.
- [44] N. Nagaosa and Y. Tokura, Topological properties and dynamics of magnetic skyrmions, *Nat. Nanotechnol.* **8**, 899 (2013).
- [45] T. Malis, S. C. Cheng, and R. F. Egerton, EELS log-ratio technique for specimen-thickness measurement in the TEM, *J. Electron Microsc. Tech.* **8**, 193 (1988).
- [46] A. N. Smith, J. L. Hostetler, and P. M. Norris, Nonequilibrium heating in metal films: An analytical and numerical analysis, *Numer. Heat Transf. A Appl.* **35**, 859 (1999).
- [47] Z. Lin, L. V. Zhigilei, and V. Celli, Electron-phonon coupling and electron heat capacity of metals under conditions of strong electron-phonon nonequilibrium, *Phys. Rev. B* **77**, 075133 (2008).
- [48] Y. Q. Li, E. K. Liu, G. H. Wu, W. H. Wang, and Z. Y. Liu, Structural, magnetic, and transport properties of sputtered hexagonal MnNiGa thin films, *J. Appl. Phys.* **116**, 223906 (2014).
- [49] B. Koopmans, J. J. M. Ruigrok, F. D. Longa, and W. J. M. de Jonge, Unifying Ultrafast Magnetization Dynamics, *Phys. Rev. Lett.* **95**, 267207 (2005).
- [50] G. P. Zhang and T. F. George, Total angular momentum conservation in laser-induced femtosecond magnetism, *Phys. Rev. B* **78**, 052407 (2008).
- [51] W. You, P. Tengdin, C. Chen, X. Shi, D. Zusin, Y. C. Zhang, C. Gentry, A. Blonsky, M. Keller, PM Oppeneer, H. Kapteyn, Z. S. Tao, and M. Murnane, Revealing the Nature of the Ultrafast Magnetic Phase Transition in Ni by Correlating Extreme Ultraviolet Magneto-Optic and Photoemission Spectroscopies, *Phys. Rev. Lett.* **121**, 077204 (2018).
- [52] A. J. McKenna, J. K. Eliason, and D. J. Flannigan, Spatiotemporal evolution of coherent elastic strain waves in a single MoS<sub>2</sub> flake, *Nano Lett.* **17**, 3952 (2017).
- [53] D. R. Cremons, D. A. Plemmons, and D. J. Flannigan, Femtosecond electron imaging of defect-modulated phonon dynamics, *Nat. Commun.* **7**, 11230 (2016).
- [54] D. J. Flannigan, D. R. Cremons, and D. T. Valley, Multi-modal visualization of the optomechanical response of silicon cantilevers with ultrafast electron microscopy, *J. Mater. Res.* **32**, 239 (2017).
- [55] O. Kovalenko, T. Pezeril, and V. V. Temnov, New Concept for Magnetization Switching by Ultrafast Acoustic Pulses, *Phys. Rev. Lett.* **110**, 266602 (2013).